Soft Matter

PAPER

View Article Online
View Journal | View Issue

Cite this: *Soft Matter*, 2022, **18**, 8194

Unmasking the structure of a chiral cubic thermotropic liquid crystal phase by a combination of soft and tender resonant X-ray scattering†

Timon Grabovac,[a] Ewa Gorecka,[b] Chenhui Zhu,[c] Damian Pociecha *[b] and Nataša Vaupotič *[ad]

Received 31st July 2022,
Accepted 15th October 2022

DOI: 10.1039/d2sm01030e

rsc.li/soft-matter-journal

A resonant X-ray scattering response for two structural models of a chiral cubic phase with a giant unit cell, one composed of a continuous grid and micelles and the other with three continuous grids, is studied theoretically and compared to experimental measurements. For both structural models resonant enhancement of all the symmetry-allowed diffraction peaks is predicted, as well as the existance of several symmetry forbidden peaks (pure resonant peaks). Experimental measurements were performed at the carbon and sulphur absorption edge. Only one pure resonant peak was observed, which is predicted by both models. Two low-angle symmetry allowed peaks, not observed in non-resonant scattering, were resonantly enhanced and their intensity angular dependence can distinguish between the two structural models.

Resonant X-ray scattering (RXS) has proven an indispensable tool to determine structures of different phases of thermotropic liquid crystals.[1,2] Because the intensity of the scattered light depends both on the spatial variation of the electron density as well as the molecular bond orientation, spatial variation of the molecular orientation can be determined from measurements. The method is based on the fact that polarizability of molecules becomes anisotropic if the energy of the incident X-ray beam is close to the absorption edge of a chemical element present in a molecule. Often, sulphur with the absorption edge at the energy 2472 eV, corresponding to the wavelength λ = 0.5 nm, is used. Carbon, being the most abundant element in organic molecules, seems like a natural choice for the resonant element, but its absorption edge is at very low energy, (283 eV, λ = 4.4 nm), thus measurements must be performed in high vacuum for the X-rays not to be absorbed by air. Recently, RXS at the carbon absorption edge (resonant soft X-ray scattering, RSoXS) proved useful to determine the structure in the twist-bend nematic phase,[3–5] its smectic analogues[6] and multi-helical smectic phases,[7–9] the structure of blue phases[4] and the structure of a two-continuous-grid cubic phase with the $Ia\bar{3}d$ symmetry (double gyroid phase).[10] The continuous-grid cubic phases with extremely large unit cells, of the order of 10 nm, are of special interest, both from the fundamental point of view as well as potential applications.[11–13] In the continuous-grid phases molecules arrange into a system of interweaving channels, each being made of linear fragments connected through multi-fold junctions. In the double gyroid phase these junctions are three-fold and planar and the planes of the neighbouring junctions are rotated by some angle. Along one grid, the rotation is clockwise and counter clockwise along the other grid, which makes the whole structure achiral. If channels accommodate elongated molecular cores, the average direction of the long molecular axes also rotates from one junction to the other.

A perplexing and extensively studied is a chiral cubic (CC) phase.[14] Upon the first observation,[15,16] chirality of the structure was not observed, and the phase was assigned an achiral $Im\bar{3}m$ symmetry. Multiple models for its structure were put forward[17,18] and their common shortcoming was that they failed to reproduce, even qualitatively, proper intensities of the peaks observed by the X-ray scattering (especially the two most intensive peaks with the Miller indices (123) and (004)). Following the discovery of the optical activity of the CC phase, the topic gained even more interest and there were several attempts to explain the origin of the phase chirality.[14,19–21] Validation of two structural models[20,21] that were proposed in

[a] *Department of Physics, Faculty of Natural Sciences and Mathematics, University of Maribor, Koroška 160, 2000 Maribor, Slovenia. E-mail: natasa.vaupotic@um.si*
[b] *Faculty of Chemistry, University of Warsaw, Żwirki i Wigury 101, 02-089 Warsaw, Poland. E-mail: pociu@chem.uw.edu.pl*
[c] *Advanced Light Source, Lawrence Berkeley National Laboratory, Berkeley, California 94720, USA*
[d] *Jozef Stefan Institute, Jamova 39, 1000 Ljubljana, Slovenia*

† Electronic supplementary information (ESI) available. See DOI: https://doi.org/10.1039/d2sm01030e

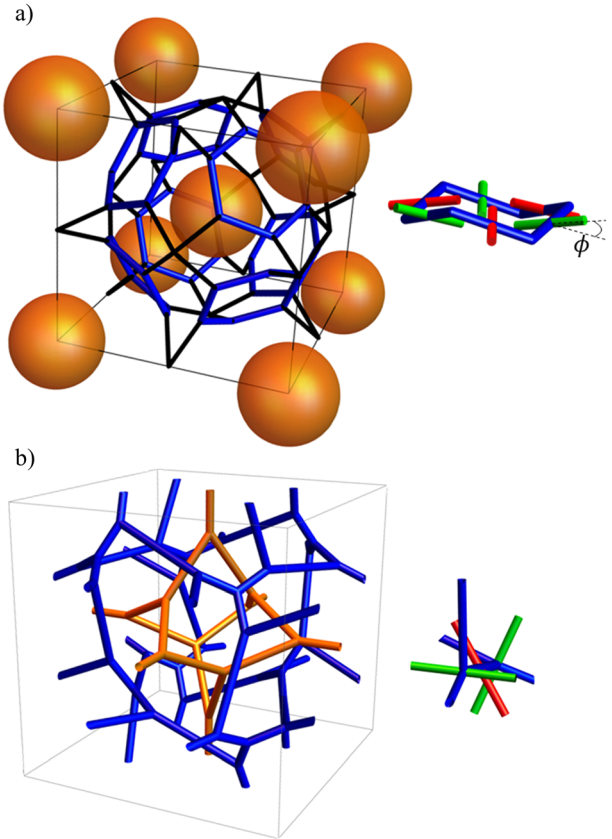

Fig. 1 Structural models of a chiral cubic phase. (a) A one-continuous-grid model with micelles.[21] Hexagons forming the grid have an arm-chair geometry; if molecules at the centre of the opposite sides of a hexagon are directed slightly up (red rods) or down (green rods), hexagons are chiral. ϕ is the angle between the line connecting the centres of the opposite hexagon sides and the direction of the long molecular axis. (b) A tri-continuous-grid model with the $I23$ symmetry.[20] The inner yellow grid repeats also in each conner of the cube, and it is not shown for the sake of picture clarity. Along each channel, long molecular axes (presented by green and red rods) twist from one junction to the other. A clockwise rotation is shown.

2020 (Fig. 1) is the major topic that the research, presented in this paper is trying to stimulate. The model presented in ref. 21 retains the original idea of the one-continuous grid model with micelles.[15] The linear segments forming the grid are arranged into eight interconnected hexagons with an arm-chair geometry. The underlying structure of channels in this model has an achiral symmetry $Im\bar{3}m$. In ref. 19 the chirality of the structure is attributed to a chiral arrangement of molecules in micelles. This should lead to a strong non-uniform density of micelles, but only a very weak inhomogeneity is detected in the X-ray diffraction data. Thus, in ref. 21, the chirality of the phase was related to a chiral ordering of molecules along the hexagon sites. Molecular cores on the opposite sides of the hexagon are slightly tilted up or down to attain more space for molecular tails (see Fig. 1a). This makes each hexagon chiral, and the best packing of molecules is achieved if all the hexagons in the unit cell have the same chirality. So far, this is the only structural model that predicts a proper ratio of intensities among the strongest peaks observed in the non-resonant X-ray scattering and a very low intensities of the peaks that are not observed experimentally (in other models the intensity of these peaks can be comparable to or even higher than for the most intensive experimentally observed peaks). The one-continuous-grid structure is closely related to a double gyroid structure. It can be formed by some minor rearrangements of the $Ia\bar{3}d$ grids because the lengths of the hexagon sides are the same as the channel segment lengths in the double gyroid phase, and so are the angles between the neighbouring sides. This is in line with the lack of a measurable enthalpy change at the transition between the chiral cubic and $Ia\bar{3}d$ phases.[22] A drawback of this model is that it contains also 8-fold junctions along the lower density channels. The model suggested in ref. 20 proposes a tri-continuous system of channels, with each grid having a chiral symmetry $I23$. Next to having a proper, chiral symmetry, the advantage of this model is that all the junctions are three-fold. But the channel segments are of different lengths than in the double gyroid phase, which requires a significant rearrangement of molecules and thus a significant enthalpy change is expected at the *CC*-$Ia\bar{3}d$ phase transition. Moreover, as seen from the ESI† in ref. 20, the model with the $I23$ symmetry predicts that the peak (114)/(033) is the second highest intensity peak, while in all the powder samples of materials

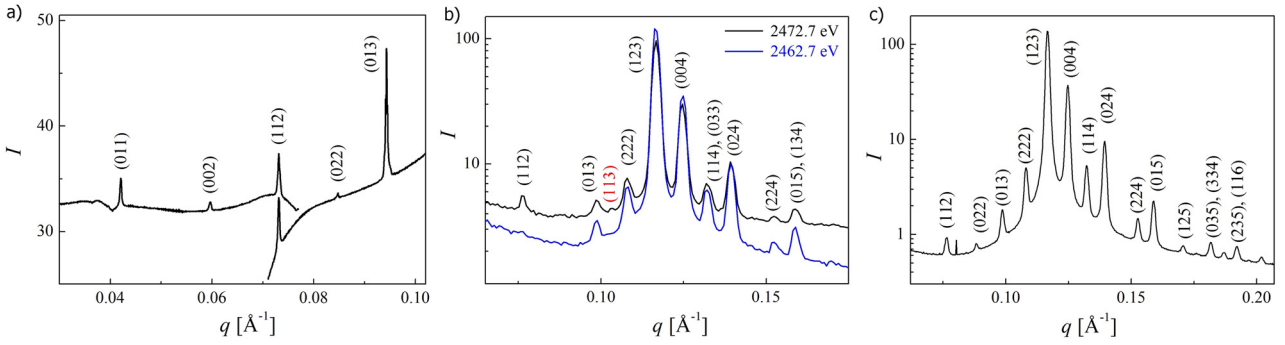

Fig. 2 Intensity of the scattered peaks as a function of the scattering wavevector magnitude (q) for the RXS measurements at: (a) the carbon absorption edge (to allow for a broader q-range two curves were recorded at different detector positions), (b) the sulphur absorption edge (black upper curve) and slightly off resonance (lower blue curve). (c) The non-resonant X-ray diffraction pattern taken with the beam energy 10 keV.

exhibiting the chiral cubic phase the peak (004) is observed to have the second highest intensity.

To validate the models of the chiral cubic phase, RXS studies can be performed, and the results should be compared to theoretical predictions for both model structures. In ref. 23 we have already calculated the intensities of the purely resonant peaks (peaks not allowed by the symmetry of the phase) and resonant enhancement of the symmetry allowed peaks for the one-continuous-grid model. Here we use the same procedure to predict the RXS response of the tri-continuous-grid model and compare theoretical predictions for both models to measurements of the RXS at the carbon (RSoXS) and sulphur (resonant tender X-ray scattering – TReXS) absorption edge.

The RXS measurements (Fig. 2) were performed for a thiophene-based bent-core policatenar mesogenic material,[21,22] showing a sequence of liquid crystalline phases CC-$Ia\bar{3}d$-$\mathrm{Col_h}$ (columnar hexagonal) on heating. In the CC phase, the resonantly enhanced peaks (011) and (002), which are not observed in a non-resonant X-ray scattering, are clearly visible by RSoXS. The TReXS experiment revealed, apart from the symmetry allowed signals, only one, very weak resonant peak (113), which disappeared at a slightly off-resonance condition.

To model the RXS response of the proposed structures we calculate the tensor form factor of the unit cell, following the procedure introduced by Pansu and Levelut.[24] We consider a cluster of molecules with their long molecular axes along a certain direction as a uniaxial anisotropic entity (scatterer) with polarizability along the average direction of the long molecular axes being different from the polarizability in the plane perpendicular to this direction. We call the eigen axis, along which polarizability is maximum/minimum the polarizability axis. Scattering properties of each scatterer are described by an anisotropic tensor, proportional to the anisotropic part of the polarizability tensor. A tensor form factor (f) in the eigen system of the scatterer is

$$f = f_0 \begin{pmatrix} 1 & 0 & 0 \\ 0 & 1 & 0 \\ 0 & 0 & -2 \end{pmatrix}$$

where f_0 is a ''strength'' of a scatterer. A tensor form factor of a unit cell, F_{uc}, is obtained by a summation over all individual scatterers; their form factors must be expressed in the same, laboratory coordinate system and the phase shift related to the position of each scatterer must be included,[23] leading to:

$$F_{\mathrm{uc}} = \sum_i f_i \mathrm{e}^{i\vec{q}\cdot\vec{r}_i}$$

where f_i is a tensor form factor of the i th scatterer positioned at $\vec{r}_i$ and $\vec{q}$ is a scattering vector.

The previous modelling of the RXS response of a double gyroid phase[10] has shown, that the major properties of the scattering pattern are obtained if a single scatterer is positioned in each centre of the channels and/or in each junction. Adding additional scatterers along the channels, such that their polarizability axes twist along the channels from one junction to the other, or additional scatterers slightly off the channel with the same direction of the polarizability axis as the scatterer in the channel (thus making the channel of a finite width with several molecules in parallel), does not bring any new peaks. To some extent it affects the intensities of the peaks, but not significantly their ratios. Due to the extreme complexity of the studied structures on one side and imperfect powder samples on the other side which enables a comparison of only major characteristics of the experimental and theoretical results, we decided to keep the simplified approach. Thus, to obtain the response of the one-continuous-grid structural model we positioned scatterers at the centre of each hexagon side, with their polarizability axes being directed toward the opposite side and slightly up or down (see Fig. 1a and ref. 23).

The tri-continuous-grid model was studied with two different configurations of anisotropic scatterers. In the first configuration, an anisotropic scatterer was positioned in each junction with the polarizability axis normal to the plane of that junction (see Fig. 3a and orientation of green rods in Fig. 1b). The second configuration assumes that scatterers are placed in the centre of channels between the junctions with the polarization axis oriented in the direction between the normal directions of the neighbouring junctions (see Fig. 3b and orientation of the red rod in Fig. 1b); it should be noted that there are two possible orientations of each scatterer, one corresponding to the clockwise rotation of the polarizability axis along the channel and the other to the counterclockwise rotation. We have studied all the possible combinations: all grids with a clockwise/counterclockwise rotation and the opposite sense of rotation on the inner/outer and middle grids.

Scattering on multiple unit cells will lead to strong diffraction only in the directions defined by the scattering vector corresponding to the Miller indices h, k and l

$$\vec{q}_{hkl} = \frac{2\pi}{a}(h,k,l)$$

where a is the length of the unit cell. To obtain intensities of the peaks, we calculate the tensor form factor of the unit cell for any combination of (hkl). These form factors have identical elements for cyclic permutations of Miller indices, which provides a neat tool to debug the computer code. The intensity is then calculated by using the procedure introduced by Dmitrienko.[25] The scattering geometry is shown in Fig. 4. For a chosen direction of the scattering vector $\vec{q}_{hkl}$, the intensity of the $\vec{\pi}$ and $\vec{\sigma}$ polarized diffracted wave was calculated, assuming a $\vec{\sigma}$ or $\vec{\pi}$ polarized incident wave. For powder samples, one must average the scattered intensity over all possible rotations of the tensor form factor around the axis defined by the scattering vector (angle φ_{q} in Fig. 4a). Next, for a chosen direction of the incident wave, a constructive interference will be observed for all the scattering vectors on the cone with the apex angle π–θ_{sc}, where θ_{sc} is a scattering angle (see Fig. 4). To obtain the total scattered intensity, we sum up the intensities at all the scattering angles on the cone. For a polarized incident wave, the crystallites with $\vec{q}_{hkl}$ on different positions on the cone will

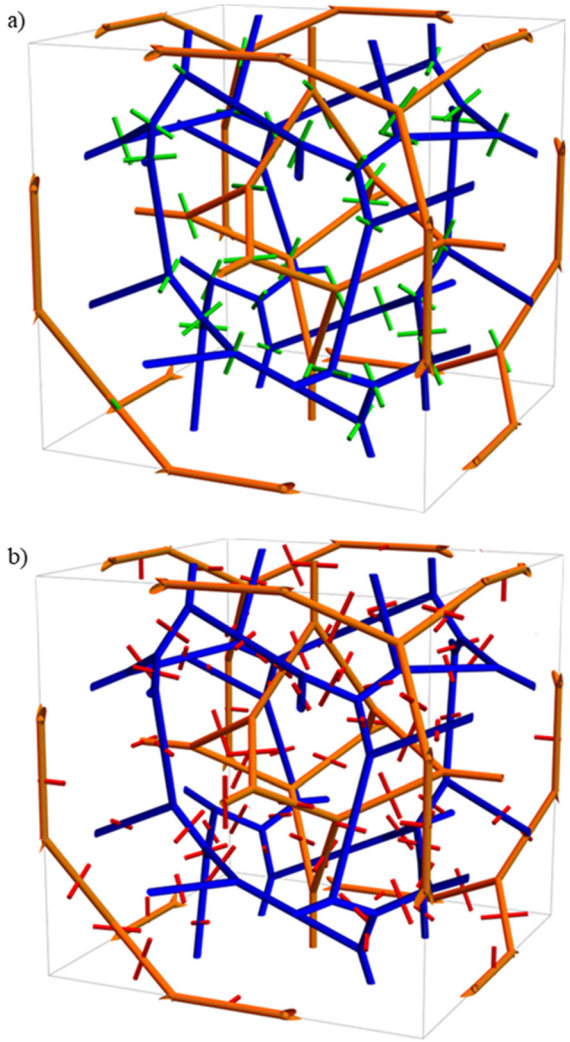

Fig. 3 Positions of scatterers inside the unit cell for the tri-continuous-grid model. (a) Scatterers (green rods) in junctions and with the polarizability axis normal to them; see also green rods in Fig. 1b. (b) Scatterers (red rods) orthogonal to channels, in their centre and with the polarizability axis along the molecular orientation at that point; see also the red rod in Fig. 1b. A clockwise rotation is chosen on both grids.

experience a different incident polarization. For example, if at the position defined by $\varphi = 0$, the incident polarization is $\vec{\pi}$, then it will be $\vec{\sigma}$ for position $\varphi = \pm\pi/2$. The intensity at a certain position on the cone can thus be obtained simply by rotating the incident polarization in the geometry shown in Fig. 4.

For both, the one-continuous grid model (OCG) with micelles and tri-continuous grid (TCG) model, we find that all the peaks allowed by the symmetry of the phase are resonantly enhanced. In addition, purely resonant peaks are also predicted. By considering the approximate experimental limitation to $h^2 + k^2 + l^2 \leq 25$, there are several purely resonant peaks predicted for both models. In the case of the OCG model the resonant peaks are due to chiral hexagons, and in the TCG model resonant peaks turn out to be all due to the scattering on the middle grid (blue grid in Fig. 1b); the inner and outer grids do not contribute (as micelles do not contribute in OCG).

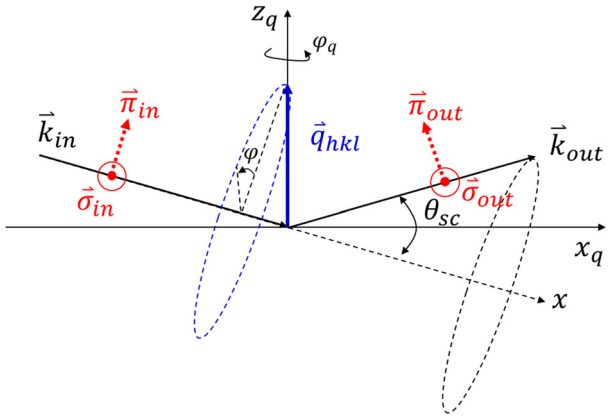

Fig. 4 The scattering geometry. The scattering vector $\vec{q}_{hkl}$ is defined by the incident ($\vec{k}_{\mathrm{in}}$, along the laboratory x axis) and scattered ($\vec{k}_{\mathrm{out}}$) wave-vectors. Polarization of the incident and scattered wave can be in the plane, defined by the scattered vector and wave vectors ($\vec{\pi}_{\mathrm{in}}$, $\vec{\pi}_{\mathrm{out}}$) or perpendicular to it ($\vec{\sigma}_{\mathrm{in}}$, $\vec{\sigma}_{\mathrm{out}}$). The angle φ that defines positions of $\vec{q}_{hkl}$ the cone is measured from the direction of $\vec{\pi}_{\mathrm{in}}$ towards the direction of $\vec{\sigma}_{\mathrm{in}}$; z_q is a direction along the vector $\vec{q}_{hkl}$ and x_q an arbitrary direction perpendicular to it; φ_q is the rotation angle around the z_q axis.

Results of intensity calculations are presented in Table 1. All the resonant peaks are given and only those resonantly enhanced peaks that are not observed in the non-resonant scattering. For a peak with Miller indices (hkl), we give the multiplicity of the peak and the total intensity for a powder

Table 1 Relative intensities of peaks with Miller indices (hkl) calculated for the TCG model with scatterers in the junctions ($I^{(J)}_{\mathrm{TCG}}$) and in centers of channels ($I^{(CCW)}_{\mathrm{TCG}}$) for the counter-clockwise rotation on all the grids, and for the OCG model (I_{OCG}). Intensities are normalized with the intensity of the peak (113). Intensities are calculated at λ_C = 4.4 nm (RSoXS) and at λ_S = 0.5 nm (TReXS). A tilt angle ϕ = 0.1 was used in the OCG model. Peaks with Miller indices (011), (002) and (233), written in bold, are symmetry allowed peaks, the rest are resonant peaks. M denotes a factor of 10^6

	(hkl)	M	$I^{(J)}_{\mathrm{TCG}}$	$I^{(\mathrm{CCW})}_{\mathrm{TCG}}$	I_{OCG}
RSoXS	(001)	6	0.14	0.13	—
	(011)	12	4.0 M	4.4 M	5.3
	(002)	6	1.4 M	19 M	10
	(012)	12	0.15	0.20	0.26
	(021)	12	0.16	0.57	
	(003)	6	0.009	0.05	—
TReXS	(012)	12	0.16	0.20	0.28
	(021)	12	0.17	0.60	
	(003)	6	0.008	0.04	—
	(113)	24	1	1	1
	(023)	12	0.12	0.27	0.34
	(032)	12	0.12	0.11	
	(014)	12	0.27	0.20	0.38
	(041)	12	0.28	0.65	
	(223)	24	0.89	0.50	1.1
	(133)	24	0.69	1.5	2.8
	(124)	24	0.12	0.64	1.1
	(142)	24	0.123	0.30	
	(233)	24	4.5 M	68 M	30
	(034)	12	0.25	0.36	0.5
	(043)	12	0.25	0.23	

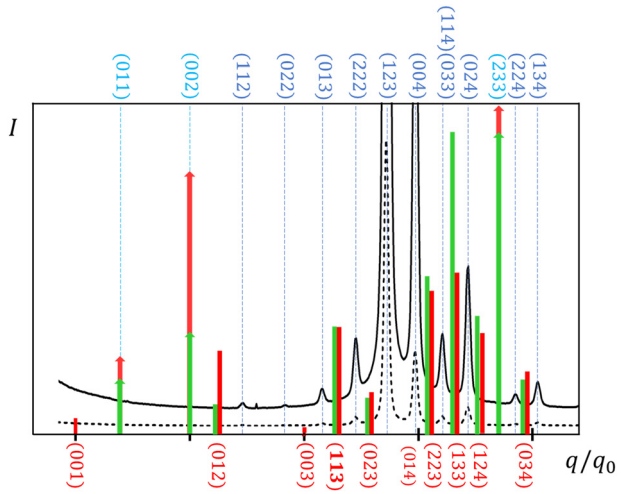

Fig. 5 Intensities (I) (in arbitrary units) of the resonant and resonantly enhanced diffraction peaks as a function of the normalized scattering vector magnitude (q/q_0), defined by the Miller indices (hkl); $q/q_0 = \sqrt{h^2 + k^2 + l^2}$. Red and green lines show the predicted peaks for the TCG and OCG model, respectively. The intensities of the resonant (lines without arrows) and resonantly enhanced (lines with arrows) peaks are not to scale (for proper ratios see Table 1, $I_{TCG}^{(CCW)}$ and I_{OCG}). The black curves show measurements by the non-resonant X-ray scattering.[11]

sample. The total intensities are normalized with respect to the intensity of the peak (113), which is the only resonant peak, observed experimentally. In the case of the OCG model, multiplicity is simply the number of all possible permutations of Miller indices. However, for the TCG model, only the peaks with cyclic permutations of Miller indices have the same intensity; if only two indices are exchanged, the intensity is different. The comparison between the results for the OCG and TCG models is given also in Fig. 5, where the positions of the resonant peaks and resonantly enhanced (011), (002) and (233) peaks are shown on the X-ray diffractogram obtained by a nonresonant X-ray scattering.[21]

From Table 1 we see that the TCG model predicts two additional resonant peaks, (001) and (003), compared to the OCG model, both for the scatterers positioned in junctions or along the channels. Although the intensities between different models cannot be directly compared because of a different number of scatterers and strong dependence of the resonant peak intensities on the chosen tilt of the polarizability axis in the OCG model, it is still striking that for the TCG model the intensities of the resonant peaks are six orders of magnitude lower than the intensities of the resonantly enhanced peaks, while for the OCG model, assuming that polarization axes are tilted by the angle $\phi = 0.1$ with respect to the line connecting the centres of the opposite hexagon sides, there is only one order of magnitude difference. If we reduce the tilt angle to $\phi = 0.01$, the intensities of the resonant peaks reduce by two orders of magnitude, while the intensities of the resonantly enhanced peaks remain the same.

Both models predict that the intensity of the experimentally observed resonant peak (113) is higher than the neighboring resonant peaks, which are not observed experimentally. These ratios are more in favour of the OCG model. The resonant peaks (001) and (003), which are predicted only by the TCG model, have much lower intensities than the peak (113), so they might be below the experimental sensitivity and their absence cannot be used for discarding the TCG model. The OCG model and the TCG model with scatterers in the centre of channels predict a strong resonant peak (133), which is also not experimentally observed. But because of a strong resonant enhancement of all the symmetry allowed peaks, the peak (133) as well as all the resonant peaks with q equal to or larger than that of the peak (023) might be hidden by the neighboring resonantly enhanced peaks. Thus, we suggest that the identification of the structure should be based on the low angle diffraction signals. Experimentally, the intensity of the resonantly enhanced peak (011) is higher than for the peak (002), which is in favor of the TCG model. However, the intensities of the resonantly enhanced peaks and their ratios strongly depend on the chosen sense of rotation along the three grids (see Table 2), while the intensities of the pure resonant peaks are unaffected by the sense of rotation. For all combinations of rotations and both models, a strong resonant enhancement of the peak (233) is predicted, but not experimentally observed.

Because only the middle grid in the TCG model contributes to the intensities of the resonant peaks, we also considered the fact that the middle grid of the TCG model consists of channels of two different lengths, which means that there is a different number of scatterers along the channels. To take this into account, we increased the strength of the scatterers at the center of longer channels, the ratio of the strengths being equal to the ratio of the channel lengths. At the same time, we also increased the strengths of the scatterers on the inner and outer grid, because these channels are also longer than the shortest channels of the middle grid. Again, this modification affected only the intensity of the resonantly enhanced peaks and their intensity ratios. The intensities of all the resonantly enhanced peaks increase, with the peak (233) always having the highest intensity and the peak (011) the lowest (see Table S1 in ESI†). The fact that the change of the scattering strength on the longer channels does not affect the intensities of the pure resonant peaks shows that only the scatterers on the shortest channels of the middle grid contribute to the onset of the pure resonant peaks.

Based on the current experimental evidence, one cannot decide on any of the two proposed structural models. Further information can be obtained by studying the angular dependence of the scattered intensity (variation of angle φ in Fig. 4) or

Table 2 Relative intensities of peaks with Miller indices (hkl) calculated for the TCG model with scatterers in centers of the channels for the counter clockwise (ccw) or clockwise (cw) rotation along the inner and outer (I/O) and middle (M) grid

(hkl)	All ccw	All cw	I/O-ccw M-cw	I/O-cw M-ccw
(011)	4.4	17	15	7.1
(002)	19	12	10	16
(233)	46	68	54	56

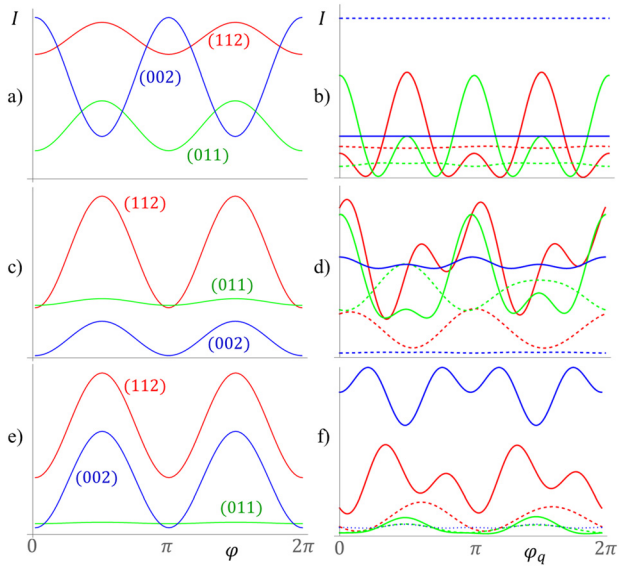

Fig. 6 Angular dependence of the scattered intensity (I) in arbitrary units for resonantly enhanced peaks (112) (red), (011) (green) and (002) (blue) for powder samples (cases (a), (c) and (e)) and for aligned samples (cases (b), (d) and (f)) for a π – (dashed lines) and σ – polarized incident wave (solid lines); (a) and (b): OCG model; (c) and (d) TCG model with scatterers in junctions; (e) and (f) TCG model with scatterers in channels, counter clockwise rotation on all the grids.

by studying well aligned samples and change, for example, angle φ_q (see Fig. 4). Because resonant peaks are predicted to be much weaker than the resonantly enhanced peaks, we propose to focus on the resonantly enhanced peaks (011) and (002), which are observed only at RXS. The peak (112) can be added as well because it disappears at out of resonance condition (see Fig. 2b) in the TReXS experiment. The angular dependence of the scattered intensity for these peaks for a powder sample is shown in Fig. 6. For the TCG model the same angular dependence is predicted for all three peaks, and qualitatively the same behaviour is observed irrespective of the rotation sense in all three grids and relative number of scatterers along the channels of various lengths (see Fig. S1, ESI†). On the contrary, for the OCG model the peak (002) has the opposite angular dependence to the peaks (011) and (112). For an aligned sample, the angular dependence is more complex. There are significant differences between the TCG model variants, the output intensity being strongly dependent also on the polarization of the incident beam (see Fig. 6 and Fig. S2, ESI†).

Conclusions

We have analysed the RXS response for two recently proposed models of a continuous grid chiral cubic phase made of polycatenar mesogenes with a giant crystallographic unit cell. We have found that both the tri-continuous-grid (TCG) and one-continuous grid (OCG) models predict resonant enhancement of all the symmetry allowed signals (Table 1 and Fig. 5) leading to measurable intensities of the diffraction peaks that are not observed at non-resonant conditions. The experimentally detected ratio of the (011) and (002) signal intensities fits only to the TCG model with scatterers in junctions; however, it should be noted that those signals were observed only by the RSoXS method, in the case of which a truly powder sample is hard to obtain. On the other hand, the (113) purely resonant signal, which is the only one observed in RXS, is the strongest according to the OCG model. The TCG model yields two resonant peaks, (001) and (003), not obtained by the OCG model, but they are predicted to be very weak.

Based on the currently available experimental evidence compared to the theoretical considerations, one cannot unambiguously validate either of the proposed structural models. We propose that the validation of the models is possible by studying the angular dependence of the resonantly enhanced peaks (011), (002) and (112), providing that a truly powder sample is realized. Validation could also be achieved by studying aligned (monodomain) samples but reaching this condition for RXS experiments might be even a more challenging task.

Author contributions

We strongly encourage authors to include author contributions and recommend using CRediT for standardised contribution descriptions. Please refer to our general author guidelines for more information about authorship.

Conflicts of interest

There are no conflicts to declare.

Acknowledgements

This research was funded by the National Science Center (Poland), grant number 2021/43/B/ST5/00240 and the Slovenian Research Agency (ARRS), through the research core funding no. P1-0055. The Advanced Light Source at the Lawrence Berkeley National Laboratory (beamlines 5.3.1, 7.3.3 and 11.0.1.2) is supported by the Director of the Office of Science, Office of Basic Energy Sciences, of the U.S. Department of Energy under Contract No. DE-AC02-05CH11231.

References

1 W. Lewandowski, N. Vaupotič, D. Pociecha, E. Gorecka and L. M. Liz-Marzán, Chirality of liquid crystals formed from achiral molecules revealed by resonant X-ray scattering, *Adv. Mater.*, 2020, **32**, 1905591.
2 Y. Cao, C. Feng, A. Jakli, C. Zhu and F. Liu, Deciphering chiral structures in soft materials *via* resonant soft and tender X-ray scattering, *Giant*, 2020, **2**, 100018.
3 C. Zhu, M. R. Tuchband, A. Young, M. Shuai, A. Scarbrough, D. M. Walba, J. E. Maclennan, C. Wang, A. Hexemer and N. A. Clark, Elucidation of Distinct Molecular Resonance Effects in Twist Bend Nematic and Smectic A Liquid Crystals *via* Tender Resonant X-ray Scattering, *Phys. Rev. Lett.*, 2016, **116**, 147803.

4 M. Salamończyk, N. Vaupotič, D. Pociecha, C. Wang, C. Zhu and E. Gorecka, Structure of nanoscale-pitch helical phases: blue phase and twist-bend nematic phase resolved by resonant soft X-ray scattering, *Soft Matter*, 2017, **13**, 6694.

5 M. Salamończyk, R. J. Mandle, A. Makal, A. Liebman-Peláez, J. Feng, J. W. Goodby and C. Zhu, Double helical structure of the twist-bend nematic phase investigated by resonant X-ray scattering at the carbon and sulfur K-edges, *Soft Matter*, 2018, **14**, 9760.

6 J. P. Abberley, R. Killah, R. Walker, J. M. D. Storey, C. T. Imrie, M. Salamończyk, C. Zhu, E. Gorecka and D. Pociecha, Heliconical smectic phases formed by achiral molecules, *Nat. Commun.*, 2018, **9**, 228.

7 M. Salamończyk, N. Vaupotič, D. Pociecha, R. Walker, J. M. D. Storey, C. T. Imrie, C. Wang, C. Zhu and E. Gorecka, Multi-level chirality in liquid crystals formed by achiral molecules, *Nat. Commun.*, 2019, **10**, 1922.

8 A. A. S. Green, M. R. Tuchband, R. Shao, Y. Shen, R. Visvanathan, A. E. Duncan, A. Lehmann, C. Tschierske, E. D. Carlson, E. Guzman, M. Kolber, D. M. Walba, C. S. Park, M. A. Glaser, J. E. Maclennan and N. A. Clark, Chiral Incommensurate Helical Phase in a Smectic of Achiral Bent-Core Mesogens, *Phys. Rev. Lett.*, 2019, **122**, 107801.

9 D. Pociecha, N. Vaupotič, M. Majewska, E. Cruickshank, R. Walker, J. M. D. Storey, C. T. Imrie, C. Wang and E. Gorecka, Photonic Bandgap in achiral liquid crystals – a twist on a twist, *Adv. Mater.*, 2021, **33**, 2103288.

10 Y. Cao, M. Alaasar, A. Nallapaneni, M. Salamończyk, P. Marinko, E. Gorecka, C. Tschierske, F. Liu, N. Vaupotič and C. Zhu, Molecular packing in double gyroid cubic phases revealed *via* resonant soft X-ray scattering, *Phys. Rev. Lett.*, 2020, **125**, 027801.

11 J. A. Dolan, B. D. Wilts, S. Vignolini, J. J. Baumberg, U. Steiner and T. D. Wilkinson, Optical properties of gyroid structured materials: from photonic crystals to metamaterials, *Adv. Opt. Mater.*, 2015, **3**, 12.

12 M. Pelanconi and A. Ortona, Nature-inspired, ultra-lightweight structures with gyroid cores produced by additive manufacturing and reinforced by unidirectional carbon fiber ribs, *Materials*, 2019, **12**, 4134.

13 E. J. Crossland, M. Kamperman, M. Nedelcu, C. Ducati, U. Wiesner, D.-M. Smilgies, G. E. Toombes, M. A. Hillmyer, S. Ludwigs, U. Steiner and H. J. Snaith, A bicontinuous double gyroid hybrid solar cell, *Nano Lett.*, 2009, **9**, 2807.

14 C. Dressel, F. Liu, M. Prehm, X. Zeng, G. Ungar and C. Tschierske, Dynamic mirror-symmetry breaking in bicontinuous cubic phases, *Angew. Chem., Int. Ed.*, 2014, **53**, 13115.

15 S. Kutsumizu, T. Ichikawa, S. Nojima and S. Yano, A cubic–cubic phase transition of 4A-n-hexacosyloxy-3A-nitrobiphenyl-4-carboxylic acid (ANBC-26), *Chem. Commun.*, 1999, 1181.

16 M. Imperor-Clerc, P. Sotta and M. Veber, Crystal shapes of cubic mesophases in pure and mixed carboxylic acids observed by optical microscopy, *Liq. Cryst.*, 2000, **27**, 1001.

17 X. Zeng, G. Ungar and M. Impéror-Clerc, A triple-network tricontinuous cubicliquid crystal, *Nat. Mater.*, 2005, **4**, 562.

18 K. Ozawa, Y. Yamamura, S. Yasuzuka, H. Mori, S. Kutsumizu and K. Saito, Coexistence of Two Aggregation Modes in Exotic Liquid-Crystalline Superstructure: Systematic Maximum Entropy Analysis for Cubic Mesogen, 1, 2-Bis (4′-n-alkoxybenzoyl) hydrazine [BABH (n)], *J. Phys. Chem. B*, 2008, **112**, 12179.

19 K. Saito, Y. Yamamura, Y. Miwa and S. Kutsumizu, A structural model of the chiral ''Im3m'' cubic phase, *Angew. Chem., Int. Ed.*, 2016, **18**, 3280.

20 X. Zeng and G. Ungar, Spontaneously chiral cubic liquid crystal: three interpenetrating networks with a twist, *J. Mater. Chem. C*, 2020, **8**, 5389.

21 N. Vaupotič, M. Salamończyk, J. Matraszek, M. Vogrin, D. Pociecha and E. Gorecka, New structural model of a chiral cubic liquid crystalline phase, *Phys. Chem. Chem. Phys.*, 2020, **22**, 12814.

22 J. Matraszek, D. Pociecha, N. Vaupotič, M. Salamończyk, M. Vogrin and E. Gorecka, Bi-continuous orthorhombic soft matter phase made of polycatenar molecules, *Soft Matter*, 2020, **16**, 3882.

23 T. Grabovac, E. Gorecka, D. Pociecha and N. Vaupotič, Modeling of the Resonant X-ray Response of a Chiral Cubic Phase, *Crystals*, 2021, **11**, 214.

24 A.-M. Levelut and B. Pansu, Tensorial x-ray structure factor in smectic liquid crystals, *Phys. Rev. E: Stat. Phys., Plasmas, Fluids, Relat. Interdiscip. Top.*, 1999, **60**, 6803.

25 V. E. Dmitrienko, Forbidden reflections due to anisotropic X-ray susceptibility of crystals, *Acta Crystallogr., Sect. A: Found. Crystallogr.*, 1983, **39**, 29.

